PHYSICAL REVIEW B **83**, 235438 (2011)

Mechanism of nanostructure movement under an electron beam and its application in patterning

Agnese Seminara,[*] Boaz Pokroy,[†] Sung H. Kang, Michael P. Brenner, and Joanna Aizenberg[‡]
Kavli Institute for BioNano Science and Technology, and School of Engineering and Applied Sciences, Harvard University, Cambridge, Massachusetts 02138, USA

(Received 21 December 2010; revised manuscript received 25 February 2011; published 30 June 2011)

In electron microscopy, the motion of the sample features due to the interaction with the electron beam has been traditionally regarded as a detrimental effect. Uncontrolled feature displacement produces artifacts both in imaging and patterning, limiting the resolution and distorting precise nanoscale patterns. The mechanism of such motion remains largely unclear. We present an experimental study of e-beam-induced nanopost movement and offer a mechanistic theoretical model that quantitatively explains the physical phenomenon. We propose that e-beam bombardment produces an uneven distribution of electrons in the sample, and the resulting electrostatic interactions provide forces and torques sufficient to bend the nanoposts. We compare the theoretical predictions with a series of controlled experiments that support our model. We take advantage of this theoretical understanding to demonstrate how this generally undesirable effect can be turned into an unconventional e-beam writing technique to generate pseudo-three-dimensional structures.

DOI: 10.1103/PhysRevB.83.235438 PACS number(s): 62.23.St, 81.65.Cf

Electron beams are widely used as a tool for characterizing the microstructure and composition of materials, with techniques ranging from low-energy electron diffraction to reflection high-energy electron diffraction, transmission electron microscopy, scanning electron microscopy (SEM), etc. In this process, the electron beam interacting with the matter results in the emission of backscattered and secondary electrons as well as electromagnetic radiation.[1] In many cases, the major portion of the injected charge remains in the material and yields undesirable effects: it alters the properties of materials, causes movement of the specimen, and leads to artifacts. An e-beam-induced feature displacement has been reported for decades and has been considered as a limiting factor both for obtaining high-resolution images[2] as well as in e-beam writing. There have been only a few studies attempting to investigate the mechanism of the movement; these include photolytically initiated solid-state chemical reactions generating pressures inside the structures,[3] shrinkage of surfaces,[4] and surface charging on thin films with one conducting layer.[5] In this paper, we propose an electrostatic model that explains feature movement and provides the basis for an unconventional, dynamic patterning technique.

I. EXPERIMENTAL OBSERVATIONS

To systematically study e-beam-induced motion of surface nanofeatures, we fabricated arrays of cylindrical nanoposts of height H and radius r [see Fig. 1(a)] from epoxy resin using soft lithography.[6] The nanoposts are attached to a supporting surface made of the same material. The samples were then sputter-coated with a 5–10-nm layer of gold or carbon, placed in a SEM and grounded. A Cressington 208 HR sputter coater and a Baltech CED 030 carbon arc coater were used for gold and carbon coating. Imaging was performed with a Zeiss Ultra 55 field-emission scanning electron microscope at Harvard Center for Nanoscale Systems. We chose high-aspect-ratio polymeric nanoposts because relatively low forces are needed to move these structures.[7] When the nanotextured surface was imaged for a few seconds in the SEM at high magnification, we observed bending of the nanoposts, as shown in Fig. 1(b). The movement pattern presents three characteristic features: (i) nanoposts near the center of the scanned region show negligible movement; (ii) maximum bending occurs at the perimeter of the scanning window; (iii) all nanoposts are bent toward the center of the scanning window. The pattern is reproducible and persists over several seconds before the nanoposts relax back to the original position, as shown by imaging a larger area. We repeated the experiment at different beam energies (1–30 KeV) and beam currents (10–150 pA). Lateral movement increases with increasing current, but surprisingly, it does not increase monotonically with beam energy: maximum bending is recorded at 5 KeV, after which the displacement decreases.

Nanopost bending strongly depends on the properties of the material, as summarized in Table I. Doped n-type silicon nanopost arrays with identical geometries showed no movement [Fig. 1(c)]. To determine whether the arrested movement results from the 20-fold increase in the bending stiffness of silicon over epoxy, we fabricated the same structures in alumina using atomic layer deposition. Although the bending stiffness of alumina is even higher than that of silicon, under the e-beam, alumina nanoposts underwent pronounced bending [Fig. 1(d)]. This rules out the hypothesis that silicon is too stiff to bend. Instead, because alumina is an electrical insulator, the experiments suggest that electrostatic interaction is responsible for bending.

II. THEORETICAL MODEL FOR THE IMPLANTED CHARGE

We thus propose an electrostatic model of nanopost bending based on a two-step process: first, electrons from the e-beam are implanted in the nanoposts as a result of backscattering; second, charging and induction produce an electric field inside the specimen, and the ensuing electrostatic forces and torques deflect the nanoposts. With this simple model, we obtain a deflection of the nanopost consistent with the experiments performed on isolated nanoposts in spot mode, and we can simply extend the prediction to nanopost arrays in scanning mode.

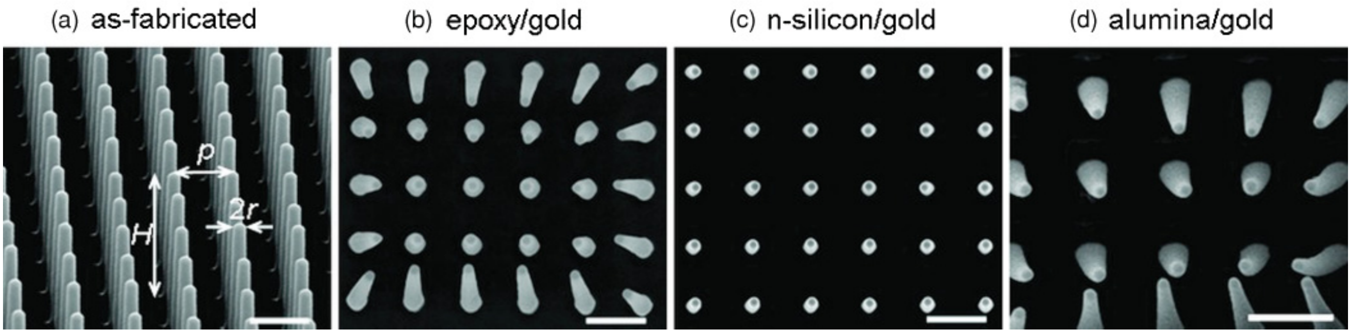

FIG. 1. Scanning electron microscope (SEM) images of samples show a reproducible movement pattern. **a**, As-fabricated nanopost array with $H = 8$ μm, $r = 0.125$ μm, $p = 2$ μm. **b**, Gold-coated epoxy nanopost arrays after ~ 1 to 5 s scanning. **c**, Gold-coated silicon nanopost arrays after $\sim$ 10 to 15 s scanning. **d**, Gold-coated alumina nanopost arrays after $\sim$10 to 15 s scanning. Scale bars 2 μm.

We first compute the magnitude of the implanted charge with a combination of theoretical arguments and Monte Carlo simulations. Simple considerations backed up by numerical simulations suggest that this implanted charge is not distributed homogeneously in the nanopost. The detailed charge distribution cannot be found by current experiments or simulations, so the theory we present has one free parameter, the center of the charge distribution. We then solve the electrostatic equilibrium problem coupled to the mechanical bending to obtain nanopost deflections in the same range as experiments.

Whenever the electron beam scans the sample, a portion of the electrons are implanted in the nearby nanoposts. For simplicity, let us consider the case of a single nanopost, with the electron beam in spot mode at a distance a from the nanopost, as sketched in Fig. 2(a). After the electron beam (with incoming current i) impacts the specimen, electrons are backscattered, with a backscattering coefficient η. Electrons backscatter at an angle θ relative to the beam direction with probability $P(\theta) = \cos\theta$ (see, e.g., Ref. 1). For a nanopost radius r and nanopost-beam distance a, a fraction $r/(\pi a)$ of these electrons impact the nanopost. Of these, a fraction η_n are further backscattered and only $1 - \eta_n$ are implanted in the nanopost, where η_n is the backscattering coefficient at the nanopost that depends on the angle of impact θ, as discussed below. The total current i_n per unit height impinging on the nanopost at a distance z from the substrate is, therefore,

$$i_n = \eta(1 - \eta_n)\frac{r}{\pi a}P(z)i, \qquad (1)$$

where $P(z) = P(\theta)|d\theta/dz| = az/(a^2 + z^2)^{\frac{3}{2}}$. If $\lambda(z,t)$ is the charge per unit height deposited at a distance z from the substrate, the charge builds up according to $\dot{\lambda} = i_n - \lambda/\tau$, where $\tau \sim \epsilon/K$ is the charge relaxation time (K is the conductivity and $\epsilon = \epsilon_0\epsilon_r$ is the permittivity; see Table I). In conditions of steady state, this yields

$$\lambda(z) = i_n(z)\tau \qquad (2)$$

with i_n given by Eq. (1). The contribution to forces and torques coming from longitudinal currents is estimated below and found to be largely negligible.

Note that the magnitude of λ and the time scale over which this steady-state charge is set up vary dramatically with material properties (see Table I). Note also that the escape depth of secondary electrons is a few nanometers, so that they are only emitted from the coating.[8,9] If the coating is grounded, charge induced by secondary emission flows rapidly to and from the ground until it reaches electrostatic equilibrium. At equilibrium, charge in the coating is determined solely by λ through electrostatic induction, and secondary emission plays no role.

III. MONTE CARLO SIMULATIONS

To quantitatively evaluate $\lambda(z)$, we obtain the backscattering coefficients η, η_n through Monte Carlo simulations of electron trajectories using an electron flight simulator available from Ted Pella, Inc. [see Fig. 2(b)]. The simulations directly provide the probability of backscattering as the fraction of electrons that backscatter and penetrate. We obtain the backscattering coefficient at primary impact η by averaging over six simulations, and we repeat the same operation at each angle of impact θ to obtain the backscattering coefficient at impact with the nanopost η_n. Note that we include in η_n the total number of electrons that either backscatter at the impact

TABLE I. Material properties and the outcome of the experiment for different materials studied.

Material	Relative permittivity ϵ_r	Bending modulus E (GPa)	Conductivity K (Ω^{-1} m^{-1})	Relaxation time scale τ (s)	Bending
epoxy	2.3	2	$\leqslant 10^{-11}$	$\geqslant 2$	yes
silicon	11.7	100	10^{-4}	10^{-8}	no
alumina	9.6	300	$\leqslant 10^{-12}$	80	yes

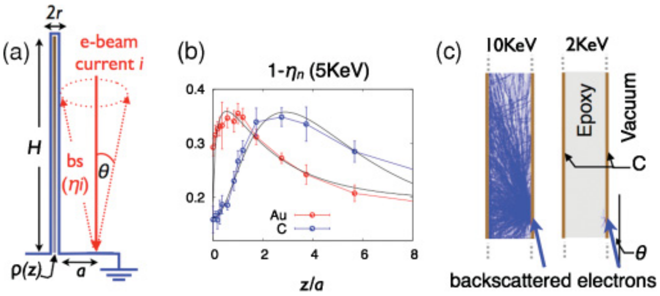

FIG. 2. (Color) Monte Carlo simulations showing charge implanted in the nanoposts after backscattering. **a**, Schematic geometry of the nanopost: after the electron beam (current i) impacts the specimen, electrons are backscattered, with backscattering coefficient η and backscattering angles θ. **b**, Implanted charge coefficient $1-\eta_n$ in the nanopost as a function of z at $E_B = 5$ KeV obtained through Monte Carlo simulations of electron trajectories using an electron flight simulator available from Ted Pella, Inc. The black lines show phenomenological fits for gold-coated samples and for carbon-coated samples, used in the simulations of nanopost bending. Error bars represent the standard deviation calculated from six different realizations of 3000 trajectories. **c**, Simulated trajectories of electrons impacting the nanopost at $\theta = 30^\circ$ for different energies (2 KeV right, 10 KeV left). The trajectories of high-energy electrons are straight lines indicating that they travel through the nanopost and leave the sample (left panel). Electrons at 2 KeV do not have enough energy to penetrate the nanopost (right panel). Optimal implant energy is intermediate. We have no access to the details of the charge distribution.

with the nanopost or travel through the thin nanopost and leave the sample from the other side.

We investigate why maximum bending occurs at an intermediate energy by repeating the simulation at different energies of the beam. In fact, depending on their energy, the electrons travel different depths in the nanopost: at energies below ~2 KeV, the electrons do not even make it inside the nanopost [Fig. 2(c), right], whereas at energies higher than ~10 KeV, electrons travel through the nanoposts and escape the sample, as suggested by the fact that most trajectories are straight lines in the left panel of Fig. 2(c). Maximum charge deposits in the nanoposts when electrons have enough energy to penetrate the nanopost but not to escape it, which explains the presence of an intermediate optimal energy for nanopost bending.

The simulations are not designed to provide detailed information on the trajectories of the electrons. However, the fact that there is an energy barrier $\Delta E \sim 2$ KeV associated with the interfaces suggests that the distribution of electrons is not uniform. Electrons that reach the outer interface with energy $< \Delta E$ are decelerated to rest before leaving the sample. We then qualitatively expect that the charge distribution is biased toward the side of the nanopost opposite to electron impact (the outer side). We parametrize these nonuniform distributions of $\lambda(z)$ by assuming that the charge is centered at a distance x_c from the axis of the nanopost. The detailed spatial distribution of the implanted electrons is beyond the scope of the present paper, so x_c is a free parameter of the model. We allow x_c to be either positive or negative, corresponding to charge accumulating toward the inner or outer side of the nanopost, i.e., the side of the nanopost exposed or opposite to the e-beam. From the above arguments, we expect $x_c < 0$: the output of the model confirms this expectation, as discussed below. We remark that although charge is also implanted underneath the point of primary impact, our simulations show that its contribution to the bending forces acting on the nanopost is negligible. (To make this point, we performed the complete numerical simulation adding a volume charge of $\eta i \tau$ at a depth of 1 μm underneath the point of primary impact in a spherical interaction volume of 0.5 μm^3. We obtained these values from Monte Carlo simulations.)

IV. THEORETICAL MODEL OF ELECTROSTATICALLY DRIVEN BENDING

We can now solve the electrostatic problem and obtain the force and torque inside the nanopost produced by the uneven charge density λ from Eq. (2) and η,η_n from Monte Carlo simulations. The equilibrium electrostatic potential ϕ is obtained by solving the Poisson equation,

$$\nabla^2 \phi = -\frac{\rho}{\epsilon}, \tag{3}$$

on the domain shown in Fig. 3(a). The implanted charge density $\rho(z)$ is distributed in a cylinder of cross section l^2 centered at a distance x_c from the axis of the nanopost [shaded area B in Fig. 3(b)], so that $\rho = \lambda / l^2$. The electrostatic force ($\mathbf{w}$) and torque ($\mathbf{N}$) per unit length of the nanopost can be computed from the action of the electric field $\mathbf{E} = -\nabla\phi$ on the static charge ρ and the induced surface charge $\sigma = \epsilon \mathbf{E} \cdot \hat{n}$, where $\hat{n}$ is the unit vector perpendicular to the coating:

$$\mathbf{N} = \int_S \rho \mathbf{E} \times \mathbf{x}\, d^2x \tag{4}$$

$$\mathbf{w} = \int_S \rho \mathbf{E}\, d^2x + r(\sigma^- \mathbf{E}^- + \sigma^+ \mathbf{E}^+). \tag{5}$$

S is the surface area of the nanopost, $\mathbf{x}$ the distance from the center of the nanopost, and the superscript + (−) denotes the side of the nanopost exposed (opposite) to the e-beam. Given the force and torque acting on the nanopost, we obtain nanopost bending by solving the equation for small bending of a thin rod:[10]

$$\frac{d\mathbf{M}}{dz} = -\mathbf{N} - \hat{z} \times \mathbf{F}, \tag{6}$$

$$\frac{d\mathbf{F}}{dz} = -\mathbf{w}, \tag{7}$$

where $\mathbf{F}$ is the shear force and $\mathbf{M}$ is the bending moment defined as $\mathbf{M} = -EI\partial_z^2 \mathbf{u}$, $\mathbf{u} = u\hat{x}$ is the displacement of the centerline, $I = \pi r^4/4$ is the area moment of inertia, and E is Young's modulus.

The electrostatic force and torque computed through Eqs. (4) and (5) are sufficient to bend epoxy nanoposts. Figures 3(c) and 3(d) show the shape of a carbon-coated nanopost at maximum bending and the maximum tip displacement as a function of x_c for both carbon- and gold-coated samples, computed through finite-element simulations. The calculations predict that the nanoposts bend inward when $x_c < 0$, i.e., when charge accumulates toward the outer side of the nanopost. We only observed inward bending for grounded

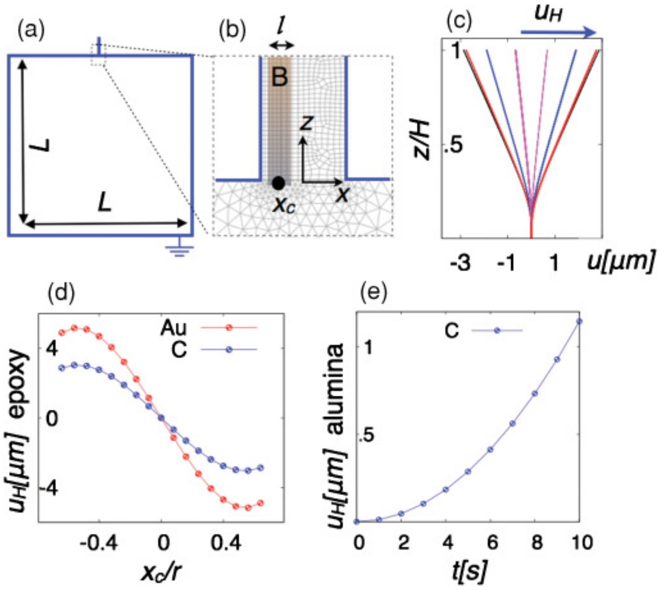

FIG. 3. (Color) Finite-element simulations of Eqs. (3)–(7) are carried out with COMSOL multiphysics on the two-dimensional domain shown in panel **a** [$\eta = 0.98$; beam current $i = 150$ pA; elastic modulus $E = 5$ GPa; beam energy $E_B = 5$ KeV; nanopost-beam distance $a = 1$ μm; results do not depend sensibly on L and l; we use $L = 0.1$ mm and $l = 0.05$ μm; $1 - \eta_n$ is given by the functions represented with black lines in Fig. 2(b)]. Since the metal coating is grounded, the potential at all external boundaries is zero. **b**, Magnification of the base of the nanopost showing the variable triangular mesh in the substrate and square mesh on the nanopost. The shaded area is charged with $\rho(z) = \lambda(z)/l^2$, where λ is given by Eq. (2). We impose $u_{z=0} = u'_{z=0} = 0$ (the base of the nanopost is clamped) and $\mathbf{M}_{z=H} = -EI\mathbf{u}''_{z=H} = -\int_S \sigma\mathbf{E} \times \mathbf{x} d^2x$; $\mathbf{F}_{z=H} = \int_S \mathbf{E}\sigma d^2x$ at the tip. **c**, Shape of a carbon-coated nanopost at maximum bending for different values of x_c between $-r$ (right) and r (left). **d**, Maximum displacement of the tip of the nanopost as a function of x_c for an epoxy specimen coated with carbon (blue) and gold (red). When charge accumulates in the outer part of the nanopost, the nanopost bends inward. **e**, Tip displacement for alumina samples coated with carbon, for $x_c = -0.08$ μm, as a function of time.

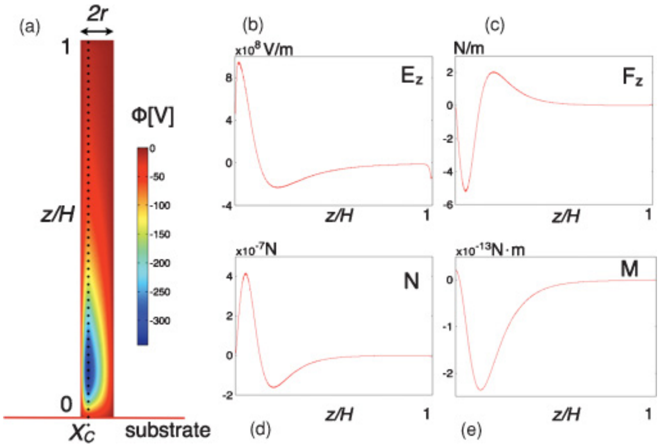

FIG. 4. (Color) **a**, Electrostatic potential ϕ obtained by finite-element simulations of Eq. (3) as described in the caption of Fig. 3 for $x_c = -0.08$ μm. **b**, Vertical electric field as a function of height, averaged over the charged portion of the nanopost [region B in Fig. 3(b)]: $E_z = -\langle \partial_z \phi \rangle$. **c**, Resulting vertical force per unit height $F_z = E_z\lambda$. **d**, Torque per unit height $N = x_c F_z$. **e**, Bending moment resulting from Eq. (6). These electrostatic forces result from the presence of both implanted charge in the nanopost and induced charge in the coating, and they yield nanopost bending, as shown in Figs. 3(c)–3(e).

samples, which implies that charge does, in fact, accumulate toward the side of the nanopost opposite to the e-beam. This prediction accords well with the intuition exposed above that the energy barrier associated with the outer interface may serve as a bias of electron distribution.

To help visualize the forces and torques bending the nanopost, we show the electrostatic potential ϕ for $x_c = -0.08$ μm in Fig 4(a). The main contribution to nanopost bending is provided by the vertical component of the electric field, whose average intensity in the charged portion of the nanopost is shown in Fig. 4(b). The resulting force per unit length $F_z = \lambda E_z$, torque per unit length $N = x_c F_z$, and bending moment M from Eq. (6) are shown in Figs. 4(c)–4(e). (Note that the interaction with the surface to which the nanopost is attached provides the external forces needed for the center of mass to shift.)

Note that to reach the steady-state charge (2), current must flow to the ground until the amount of charge that is implanted in each portion of the nanopost i_n equals the amount of charge λ/τ that flows to the ground through the coating. We neglect

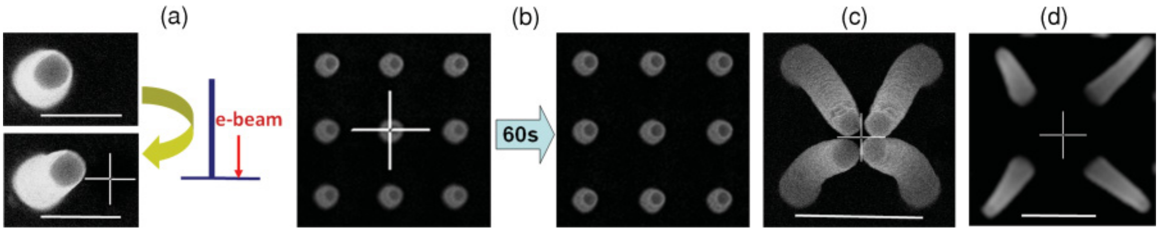

FIG. 5. (Color online) SEM images showing experimental tests of the proposed model. All samples are made of epoxy coated with gold and grounded (unless otherwise specified). **a**, Position of a single nanopost before (top) and after (bottom) exposure to the e-beam in spot mode. The position of the e-beam is marked with a white cross, and a schematic for the edge-on view is shown to the right. **b**, Image of a sample before (left) and after (right) 60 s exposure to the e-beam in spot mode focused on the center of a single nanopost. The position of the e-beam is marked with a cross. **c**, Inward bending and tetramer formation upon focusing the e-beam in the center of four nanoposts coated with gold and disconnected from the ground. **d**, Outward bending of four nanoposts coated with carbon and disconnected from the ground. Scale bars are 1 μm for **a**, 2 μm for **c** and **d**.

the contribution to forces and torques originating from these longitudinal currents because they are largely smaller than the static components. This is easily seen by estimating the current density flowing to the ground $J \lesssim i_n/\xi^2$, where ξ is the thickness of the coating, generating an electric field $E_{||} \sim J/K$, where K is the conductivity of the coating. $E_{||}$ acts on the static charge $\lambda_{\mathrm{ind}} \sim \lambda$ induced in the coating by the implanted charge λ, yielding a torque per unit height $T \sim \lambda_{\mathrm{ind}} E_{||} r \approx 10^{-18}$ nN, where we have used the values of r, a, and H in the caption of Fig. 1; $K \approx 10^7\ \Omega^{-1}\,\mathrm{m}^{-1}$, $\tau \approx 1$ s, and $i \approx 150$ pA. In fact, the torque originating from the static charge ranges from $N \sim 400$ nN close to the base of the nanopost to about 1 nN at the tip [see Fig. 4(d)], with an average of about 0.1 nN, so that we can largely neglect the contribution coming from these nonequilibrium effects.

V. COMPARISON WITH EXPERIMENTS AND APPLICATION TO PATTERNING

The theory for the bending of a single nanopost is sufficient to explain the patterns observed in scanning mode actuation shown in Fig. 1(b). Here the scanning is so rapid that charge distributes simultaneously over many nanoposts. Nanoposts on the edges are only exposed to the electron beam from the inside of the scanned area. Similar to the case of an isolated nanopost, these electrons accumulate toward the outside of the nanoposts yielding maximum inward bending. Maximum displacement at the tip of these nanoposts is of $\sim 2\ \mu$m, as seen from Fig. 1(b), which agrees well with our prediction for $x_c \sim 0.2\ \mu$m [see Fig. 3(d)].

In contrast, symmetry breaking is washed out for nanoposts located near the center of the scanned region, since these receive about the same number of backscattered electrons from all directions. Here we expect $x_c \sim 0$ and no bending. The measured time scale of bending is a few seconds (see the caption of Fig. 1), consistent with our theoretical estimate for $\tau = 2$ s.

The model also explains the behavior of silicon and alumina samples. Since the implanted charge is proportional to τ [Eq. (2)], and τ for doped-silicon is eight orders of magnitude smaller than for epoxy (Table I), we predict negligible bending for silicon nanoposts, consistent with the experimental observation shown in Fig. 1(c).

For alumina, because of the long time scale for charge equilibration, $\tau \approx 80$ s, we assume that charge builds up linearly in time, and we perform a quasistatic analysis as a function of time. Figure 3(e) shows that the electrostatic force is strong enough to even bend alumina nanoposts. We predict that a 1 μm deflection of the tip, equivalent to deflection of epoxy nanoposts, is reached upon waiting for ≈ 10 s [see Fig. 3(e)]. This was experimentally verified, as shown in Fig. 1(d).

Further experiments corroborate the theoretical expectations. The theory shows that nanopost actuation does not require interaction between nanoposts, and an isolated nanopost is expected to be deflected by the electron beam. In fact, we verify experimentally that if we focus the e-beam near an isolated nanopost, the nanopost bends toward the e-beam [Fig. 5(a)]. We can further validate this prediction by focusing the e-beam in the center of a nanopost: in this case, where there is no symmetry breaking in electron distribution, we observe no bending [Fig. 5(b)]. Moreover, we expect that the direction of nanopost deflection may be reversed. In all of the above arguments, we considered grounded samples for which charge in the coating is determined solely by electrostatic induction, as discussed above. However, if the ground is removed, the magnitude and sign of the charge in the coating should depend on secondary emission (SE).[11] A switch in the sign of the

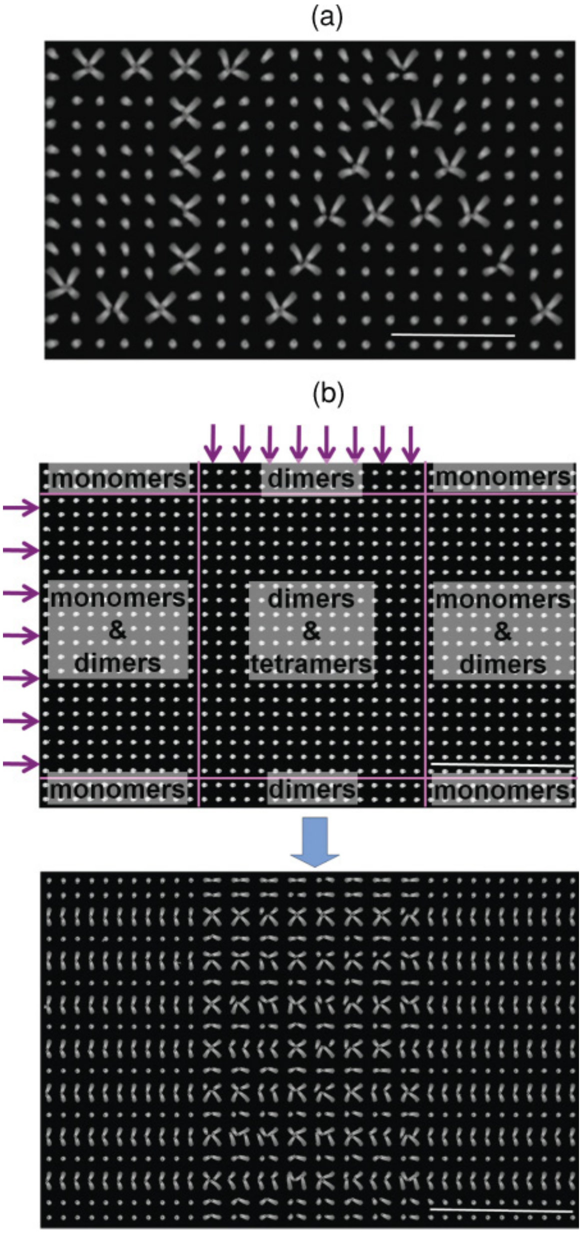

FIG. 6. (Color online) SEM images showing applications for patterning. The samples are made of epoxy coated with gold and grounded. **a**, Writing of letters in nanopost arrays through repeated exposure to the e-beam in spot mode. **b**, Controlled patterning of the nanopost array by seven horizontal line scans (skipping one row in between scans) and eight consecutive vertical scans, shown on the left micrograph. The first scan always produces dimers; an additional scan perpendicular to the existing dimers produces tetramers, shown in the micrograph on the right. Scale bars are 10 μm for **a** and 20 μm for **b**.

charge in the coating may reverse the electric field inside the nanopost, thus yielding outward bending. Direct numerical simulations of the ungrounded case are not possible because they couple length scales that range from the nanometer to the millimeter. (Note that in the grounded case, the coating is simply modeled as a $V = 0$ surface, and because the electric field outside the sample vanishes, there is no need to resolve the details of electric-field variation inside the coating.) Although we have no access to the detailed charge distribution, we expect that materials with very different secondary yields may behave in opposite ways. In fact, upon removing the ground, the gold-coated samples (SE coefficient 0.7) show inward bending whereas carbon-coated samples (SE coefficient 0.05) show outward bending [Figs. 5(c) and 5(d)]. Note that these results rule out the possibility that thermal expansion or electromagnetic forces are the mechanism causing bending.

In light of our findings and modeling, we believe that e-beam-induced nanopost bending can be used as a powerful patterning technique. To demonstrate this technique, we fix the e-beam at one position between two or four nanoposts. Our model predicts that the backscattered electrons accumulate in the external part of each nanopost and they all move independently toward the e-beam. (Grounding eliminates the electrostatic field outside the sample, so that the nanoposts only interact inside the material. Because of screening, this interaction is negligible, as confirmed by simulations.) Experiments confirm this prediction and additionally show that when the nanopost tips come into contact, they ultimately stick to each other. (The mechanism for adhesion between the nanopost is beyond the framework of the present study, but it is most probably due to van der Waals interaction.[14]) Based on this result, we are able to perform larger-scale patterning or "writing" of clusters by repeated point [Fig. 6(a)] or line [Fig. 6(b)] scans. The strength of the proposed technique is that it can be done in any SEM, with no need or a special apparatus that, e.g., standard e-beam writing requires. Additionally, the minimum required voltage is about 4 KeV, which is a standard value, while e-beam writing techniques may require voltage as high as 90 KeV. This minimum value can be further lowered by engineering properly the coating thickness and the material.

In summary, this work presents a study of the physical mechanism of e-beam-induced specimen movement and demonstrates how this process can be controlled to yield arbitrary arrays of surface clusters. Beyond fundamental physical insight, this new dynamic e-beam writing technique can prove useful for nanomechanical memories. By producing the arrays of nano- or micron-sized mechanical cantilevers[12] resilient to electromagnetic fields,[13] one can potentially achieve data storage beyond superparamagnetic limits (100 Gb/in^2) with low-level power consumption.

ACKNOWLEDGMENTS

This work was supported by the Kavli Institute for Bionano Science and Technology at Harvard University, the Materials Research Science and Engineering Center under NSF Award No. DMR-0820484 and the NSF Award No. DMS-0907985. We acknowledge the use of the facilities at the Harvard Center for Nanoscale Systems supported by NSF Award No. ECS-0335765. A.S. was supported by a Marie Curie International Outgoing Fellowship within the 7th European Community Framework Programme.

---

[*] Current address: Institut Pasteur, Department of Genetics and Genomics, 28 rue du Dr. Roux, 75015 Paris, France.

[†] Current address: Department of Materials Engineering and the Russell Berrie Nanotechnology Institute,Technion–Israel Institute of Technology, Haifa 32000, Israel.

[‡] Corresponding author: jaiz@seas.harvard.edu

[1] J. Goldstein *et al.*, *Scanning Electron Microscopy and X-ray Microanalysis* (Plenum, New York, 1992).

[2] R. Henderson and R. M. Glaeser, Ultramicroscopy **16**, 139 (1985).

[3] R. M. Glaeser, J. Struct. Biol. **163**, 271 (2008).

[4] T. I. Kim, H. E. Jeong, K. Y. Suh, and H. H. Lee, Adv. Mater. **21**, 2276 (2009).

[5] R. M. Glaeser and K. H. Downing, Microsc. Microanal. **10**, 790 (2004).

[6] B. Pokroy, A. K. Epstein, M. C. M. Persson-Gulda, and J. Aizenberg, Adv. Mater. **21**, 463 (2009).

[7] A. R. Ragab and S. E. A. Bayoumi, *Engineering Solid Mechanics: Fundamentals and Applications* (CRC, Boca Raton, FL, 1998).

[8] J. Cazaux, J. Electron Spectrosc. Relat. Phenom. **105**, 155 (1999).

[9] J. Cazaux, X-Ray Spectrom. **25**, 265 (1996).

[10] L. Landau and L. Lifshitz, *Theory of Elasticity* (Addison-Wesley, Reading, MA, 1959).

[11] J. D. Jackson, *Classical Electrodynamics* (Wiley, New York, 1962).

[12] P. Vettiger *et al.*, IEEE. Trans. Nanotechnol. **1**, 39 (2002).

[13] R. L. Badzey, G. Zolfagharkhani, A. Gaidarzhy, and P. Mohanty, Appl. Phys. Lett. **85**, 3587 (2004).

[14] B. Pokroy, S. H. Kang, L. Mahadevan, and J. Aizenberg, Science **323**, 237 (2009).